Yabe, Y., Nakatani, M., Naoi, M., Philipp, J., Janssen, C., Watanabe, T., Katsura, T., Kawakata, H., Dresen, G., Ogasawara, H. (2015): Nucleation process of an M2 earthquake in a deep gold mine in South Africa inferred from on-fault foreshock activity. - *Journal of Geophysical Research*, *120*, 8, pp. 5574—5594.

DOI: http://doi.org/10.1002/2014JB011680

AGU PUBLICATIONS

JGR

Journal of Geophysical Research: Solid Earth

RESEARCH ARTICLE
10.1002/2014JB011680

Key Points:
- Foreshock distribution clearly delineates the main shock rupture plane
- Persistent clusters of foreshocks suggest quasistatic preparation at multiple sites
- Strength heterogeneity control of the preparation process of the main shock

Correspondence to:
Y. Yabe,
yasuo.yabe.e2@tohoku.ac.jp

Citation:
Yabe, Y., M. Nakatani, M. Naoi, J. Philipp, C. Janssen, T. Watanabe, T. Katsura, H. Kawakata, D. Georg, and H. Ogasawara (2015), Nucleation process of an M2 earthquake in a deep gold mine in South Africa inferred from on-fault foreshock activity, *J. Geophys. Res. Solid Earth*, *120*, 5574–5594, doi:10.1002/2014JB011680.

Received 10 OCT 2014
Accepted 5 JUL 2015
Accepted article online 14 JUL 2015
Published online 6 AUG 2015

Nucleation process of an M2 earthquake in a deep gold mine in South Africa inferred from on-fault foreshock activity

Yasuo Yabe[1], Masao Nakatani[2], Makoto Naoi[3], Joachim Philipp[4], Christoph Janssen[5], Takayoshi Watanabe[1,6], Taishi Katsura[7,8], Hironori Kawakata[7], Dresen Georg[5], and Hiroshi Ogasawara[7]

[1]Research Center for Prediction of Earthquakes and Volcanic Eruptions, Graduate School of Science, Tohoku University, Sendai, Japan, [2]Earthquake Research Institute, the University of Tokyo, Tokyo, Japan, [3]Department of Civil and Earth Resource Engineering, Graduate School of Engineering, Kyoto University, Kyoto, Japan, [4]GMuG Gesellschaft für Materialprüfung und Geophysik, Bad Nauheim, Germany, [5]GFZ German Research Centre for Geosciences Helmholtz Centre Potsdam, Potsdam, Germany, [6]Now at Japan Atomic Energy Agency, Ibaraki, Japan, [7]College of Science and Engineering, Ritsumeikan University, Kusatsu, Japan, [8]Now at Hitachi Solutions, Ltd., Tokyo, Japan

Abstract Using a network of sensitive high-frequency acoustic emission sensors, we observed foreshock activity of an Mw 2.2 earthquake (main shock) in a deep gold mine in South Africa. Foreshock activity, which selectively occurred on a part of the rupture plane of the forthcoming main shock, lasted for at least 6 months until the main shock. Rock samples recovered from the main shock source region showed evidence of ancient hydrothermal alteration on the main shock rupture plane, suggesting that the foreshock activity occurred on a preexisting weakness. The foreshocks during 3 months before the main shock were concentrated in three clusters (F1–F3), which we interpret as representing localized preslip at multiple sites. While the location of mining area, the source of stress perturbations, changed with time, the locations of foreshock clusters did not change, suggesting that the preslip patches were controlled by strength heterogeneity rather than stress distribution. Activity over the entire foreshock area was generally constant, but the largest cluster (F2) showed accelerated activity starting at least 7 days before the main shock, while mining stress did not increase in this period. The main shock initiated at a point close to F1, away from F2. All the six foreshocks during the final 41 h occurred in F1 and F2 and in-between. These suggest that in the last stage of the preparation process of the main shock, preslip patches interacted with each other through the stress concentration ahead of the expanding preslip patch (F2), which should be the only driving force of the preparation process under the constant external load.

1. Introduction

Stick-slip experiments in laboratories have revealed that shear instability on a fault is preceded by a preparation process, referred to as quasistatic nucleation [e.g., *Okubo and Dieterich*, 1984; *Ohnaka and Kuwahara*, 1990]. Based on stick-slip experiments using large rock samples, *Ohnaka and Kuwahara* [1990] divided the preparation process of dynamic instabilities into three phases: (I) the static formation of a preslip patch, (II) subsequent quasistatic growth of the patch as the external load increases, and (III) still stable but accelerating growth up to a critical patch length at which dynamic instability begins. The process in phase III proceeds without an increase in external load. After the patch length reached the critical length, the growth rate of the preslip patch farther accelerates to a terminal speed of about 80–90% of *S* wave speed. The seismic wave radiated during the acceleration of growth rate to the terminal speed is sometimes called the nucleation phase [e.g., *Ellsworth and Beroza*, 1995]. To distinguish the dynamic process that radiates seismic waves and the aseismic or quasistatic nucleation processes (up to phase III of *Ohnaka and Kuwahara* [1990]), we refer to the former process as the dynamic nucleation and the latter processes as the preparation process or the quasistatic nucleation in the present paper.

The preparation process of dynamic instability, which is also expected from Griffith's energy balance theory of fracture mechanics, has been reproduced by numerical simulations assuming either rate and state friction [*Dieterich*, 1992; *Rice*, 1993] or slip-weakening friction [*Shibazaki and Matsu'ura*, 1998]. Because an earthquake represents dynamic shear instability on a fault, either within Earth's crust or at a plate interface, a similar

preparation process (to that indicated by laboratory and numerical studies) is expected to precede natural earthquakes, resulting in a change in the state of the fault from locked to spontaneously propagating dynamic slip. Preparation process is therefore one of the core issues in understanding earthquake generation. Furthermore, because the preparation process is accompanied by aseismic sliding (or preslip) and aseismic sliding usually involves friction noise or microseismicity on a fault [e.g., *Yabe et al.,* 2003; *Thompson et al.,* 2005; *McLaskey and Lockner*, 2014] (i.e., local instabilities at scales much smaller than that of a preslip patch), foreshock activities could be a manifestation of the preparation process [e.g., *Jones and Molnar*, 1979; *Dodge et al.,* 1995, 1996; *Yamaoka et al.,* 1999; *Umino et al.,* 2002; *Okada et al.,* 2007; *Yukutake et al.,* 2008; *Kato et al.,* 2012].

Active, deep mines provide an excellent opportunity for observing earthquake preparation processes, because the spatial and temporal scales involved are intermediate between those of natural earthquakes and typical laboratory experiments. As importantly, many earthquakes in these mines occur close to the observation sites, and they occur on geological structures rather than on the artificial faults used in the laboratory [e.g., *Mendecki*, 1996; *Young et al.,* 2000; *Richardson and Jordan*, 2002; *Naoi et al.,* 2014, 2015a, 2015b]. In deep gold mines in the Republic of South Africa (RSA), relatively large events (up to ~M3) take place near the advancing mining front, where stress changes for a few years may exceed tens of MPa [*Chamber of Mines Research Organization (COMRO),* 1988]. Therefore, utilizing the geological information and the mining plan, we developed a very sensitive seismic network at a depth of about 3.3 km in Mponeng gold mine, Carletonville, RSA, to precisely observe acoustic emission (AE) activity, i.e., microseismicity that is not detected by the ordinary seismic network operated by the mining company [*Nakatani et al.,* 2008]. On 27 December 2007, ~6 months after installation of our network, an earthquake of Mw 2.2 (hereafter, the main shock) occurred ~30 m above our network [*Yabe et al.,* 2009; *Naoi et al.,* 2011]. We successfully observed AE activity during the 6 months leading up to the main shock.

Hauksson [2010] and *Powers and Jordan* [2010] have pointed out that most seismicity along major faults does not actually occur on the fault but in "the fairly broad damage zone" within the host rock [*Chester et al.,* 1993] surrounding the fault. In such situations, it is practically difficult to recognize changes in seismicity associated with the quasistatic nucleation (preslip) on the fault core [*Chester et al.,* 1993], by distinguishing them from the fluctuation of higher seismicity in the damage zone or background. In contrast, the AE activity that we observed for 6 months prior to the main shock was concentrated to the future rupture plane of the main shock, as delineated by a tightly constrained planar concentration of more than 10,000 aftershocks occurring within 150 h following the main shock. As shown later, the main shock seems to have occurred on a preexisting weak plane in a rather intact rock mass unlikely containing a well-developed damage zone. Therefore, we conduct in-depth examination to see if we can find any signs of the quasistatic preparation process (spatial and temporal evolutions of localized preslip) that proceeds on the future rupture plane of the main shock.

2. Observations

Details of the observation network, characteristics of the main shock, and the characteristics of the aftershock activity are described in previous papers [*Nakatani et al.,* 2008; *Yabe et al.,* 2009; *Naoi et al.,* 2011]; we briefly review them below.

2.1. Observation Site

The observation network was deployed at a depth of ~3.3 km along an access tunnel traversing a vertical, gabbroic dike, called the Pink and Green (PG) dike, and quartzite host rock (Figure 1). The tabular reef in the mine is in the host rock and dips to the SSE at ~26.5°. Our observation site was 90 m below the reef. Tabular mining to the west of the PG dike was completed before the observation period, which started in June 2007; the reef to the east of the PG dike was mined after the observations started. The PG dike was unmined and was left as a pillar supporting a substantial roof load [*Hofmann et al.,* 2012, 2013; *Yabe et al.,* 2013; *Ogasawara et al.,* 2013, 2014].

Many boreholes had been drilled near our observation site by the mining company prior to installation of the observation network, for the purpose of mine planning. No faults with significant offset were found. Therefore, the PG dike was largely intact. However, no boreholes passed through the rupture plane of the

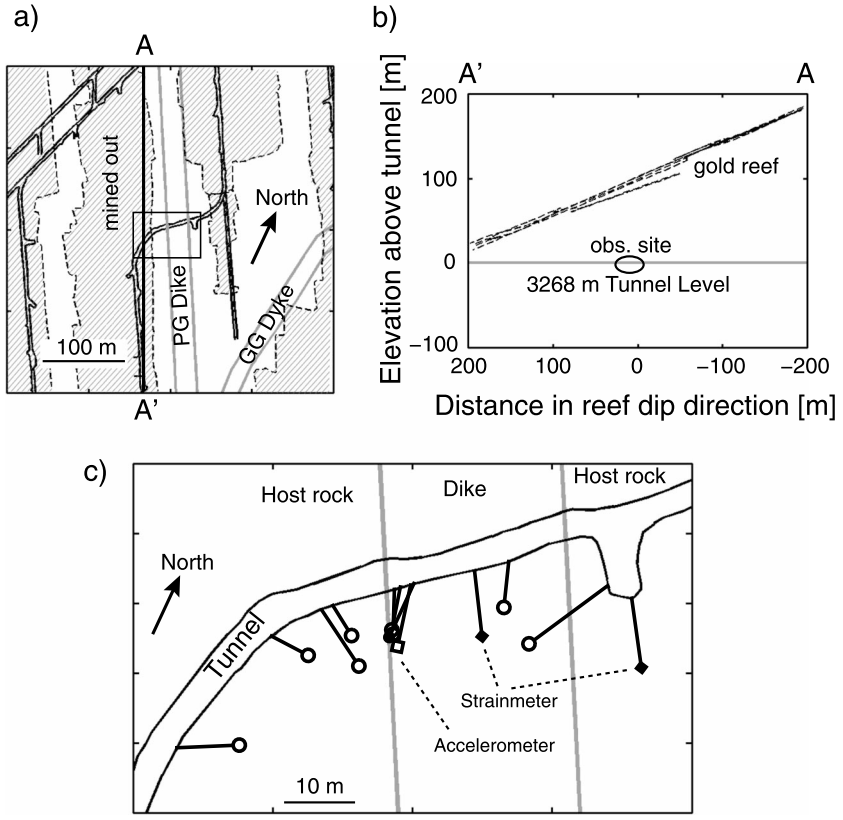

Figure 1. (a) Map of the observation area in a deep gold mine in RSA. Shaded areas indicate a gold reef that was mined out before December 2007. The reef is about 90 m above our observation site and dips to the SSE at ~26.5°. (b) Cross section of our observation area parallel to the dip of the reef around our network that is deployed along an access tunnel at a depth of 3268 m from the ground surface. (c) A close-up view of the network. The location is indicated by the box in Figure 1a. Solid lines indicate boreholes in which sensors were installed. Open circles and a solid circle denote AE sensors having a response of up to 200 kHz and 100 kHz, respectively. The open square and solid diamonds denote a three-component accelerometer and three-component Ishii strainmeters, respectively.

main shock before it occurred. Approximately 1 year after the main shock, we drilled a 90 m long borehole that intersected the rupture plane of the main shock to investigate the rock properties of the source region.

2.2. Observation Network

The observation network consisted of eight high-frequency AE sensors, one triaxial accelerometer, and two Ishii strainmeters. Seven of the eight AE sensors cover a frequency range from about 1 kHz to 200 kHz, with moderate resonances at about 70 kHz and 130 kHz. The other AE sensor covers up to 100 kHz. The accelerometer has flat frequency characteristics from 2 Hz to 25 kHz. The sensors were installed in boreholes of 6–15 m length to reduce attenuation in the zone of rocks damaged by tunnel excavation. The waveforms were fed to 16-channel GMuG AE observation system having a resolution of 16 bits [e.g., *Manthei*, 2005]. Analogue signals were band-pass filtered and amplified by 0–20 dB before digitization at 500 kS/s. The recording was on trigger mode. Upon trigger, an in situ location algorithm was invoked, and automatically picked *P* and *S* wave arrival times were recorded on a hard disk drive (HDD) of the observation system. Waveform storage was optional. When this option was on, waveforms of ~65 ms (32,768 samples) were kept on the HDD. The smallest magnitude (Mw) of AE events determined by this network was Mw −4.4 [*Kwiatek et al.,* 2010]. Note that AE events with magnitudes less than Mw −4.4 were located well, although their magnitudes could not be determined because of low signal-to-noise ratios.

Network observations were interrupted from late June to the end of August due to failures of the recording system. To save disk space of HDD, waveforms were kept only for the AE events that occurred during the following six time windows: (1) 13–17 June (100.7 h), (2) 12–14 September (28.8 h), (3) 3–6 October (44.3 h),

(4) 10–13 December (26.1 h), (5) 15–19 December (64.2 h), and (6) 24–27 December (65.4 h). We did not record waveforms in daytime from 12 September to 19 December, to avoid filling the HDD with mining noise such as continuous vibrations from drilling. During 13–17 June and 24–27 December, waveform recordings were enabled throughout; the former period was during the initial phase of our observations, when we were evaluating contamination of our recordings by mining noise, whereas the latter was during a holiday from 21 December to 1 January, during which no mining noise was generated.

Even during the periods when waveform recording was disabled, the arrival times of *P* and *S* waves were automatically picked by an in situ waveform analysis upon all triggers and were stored, for 24 h per day from October 3 to the main shock, except for the period of 11–21 October when the network was inoperative. Therefore, the automatically picked arrival times are available for examining long-term AE activity for about 3 months leading up to the main shock, though they are likely to be less accurate than the manually picked arrival times. The periods when the manually picked arrival times and the automatically picked arrival times are available, as well as the modeled stress state [*Hofmann et al.,* 2012] on the rupture plane of the main shock, are summarized in Table 1 (see also Figure 8a).

2.3. Main Shock and Aftershocks

The main shock (Mw 2.2) occurred near our observation site on 27 December 2007 [*Yabe et al.,* 2009; *Naoi et al.,* 2011]. *Naoi et al.* [2011] manually picked *P* and *S* wave arrival times to locate more than 20,000 AE events that occurred within 150 h following the main shock. The location error for events within ~40 m of the center of the network was 1 m or less. The aftershocks clearly delineated a plane (aftershock plane) in the PG dike with a strike of N22W and a dip of 68° toward N68E (Figures 2 and 3). Since waveform of the main shock recorded by our network was saturated, *S* wave arrival times of the main shock could not be picked. *Naoi et al.* [2011] compared *P* wave arrival times of the main shock with those of well-located aftershocks to locate the hypocenter of the main shock relative to the aftershocks. The obtained main shock hypocenter was about 30 m above our network and on the aftershock plane. They determined a focal mechanism solution of the normal fault for the main shock using seismic waveforms recorded by the seismic network operated by the mine. One of the nodal planes agreed well with the aftershock plane. Therefore, the aftershock plane is considered to correspond to the rupture plane of the main shock.

Strain changes in the source region were measured by two triaxial strainmeters, one installed in the PG dike and one in the host rock, from June 2007 [*Katsura*, 2009; *Ogasawara et al.,* 2013]. The smallest distance from the strainmeters to the rupture plane of the main shock was less than 10 m. The strain monitoring showed increases in the subvertical compression of 18 MPa in the PG dike and 11 MPa in the host rock. The rupture plane of the main shock, which was optimally oriented with respect to the stress state expected for a region around active mining, fell within a region of marked stress concentration [*Hofmann et al.,* 2012, 2013; *Yabe et al.,* 2013].

3. Results

3.1. Investigation of Drilling Core Samples

Drilling of a borehole passing through the source region of the main shock started about 1 year after the main shock and took ~6 months to complete. The borehole intersected the aftershock plane 8 m south of the main shock hypocenter (Figures 4a and 4b). We recovered core samples from the entire length of the borehole except for in a 10 m section of the hanging wall of the main shock rupture plane, where core samples were severely crushed into small pieces, suggesting a larger differential stress in the hanging wall.

From the recovered drilling core samples, we selected four specimens from the footwall and five specimens from the hanging wall, within 10 m and 16 m, respectively, of the rupture plane of the main shock. Two of the five specimens from the hanging wall were collected from the 10 m long section of crushed rock; therefore, the original locations of these two specimens are ambiguous. One additional specimen was selected from the drilling core samples recovered from where it intersected the rupture plane of the main shock. Therefore, the original location of this specimen was probably on the rupture plane of the main shock. The 10 specimens were examined by optical microscopy and scanning electron microscopy, and were analyzed using X-ray diffraction (XRD) and energy dispersive X-ray spectrometry.

Journal of Geophysical Research: Solid Earth

10.1002/2014JB011680

Table 1. Data Availability and Products

	Jun	Jul	Aug	Sep	Oct	Nov	Dec	Products
Manual picks	All day for 13–17 (100.7 h)	N/A	N/A	Nighttime for 12–14 (28.8 h)[a]	Nighttime for 3–6 (44.3 h)[a]	N/A	Nighttime for 10–13 (26.1 h) and 15–19 (64.2 h) All day for 24–27 (65.4 h)	Figure 2 Figure 3 Figures 4a and 4b Figure 5 Figure 6 Figure 7 Figure 8 Figure 10 Figure 11 Figure 12 Figure 13
Automatic picks	N/A	N/A	N/A	N/A	Fully available for 3–10 and 22–31	Fully available	Fully available until the main shock	Figure 5 Figure 6 Figure 7 Figure 8 Figure 10 Figure 11 Figure 12 Figure 13
Normal stress, MPa[b]	N/A	53.36	53.56	53.67	53.75	53.80	N/A	
Shear stress, MPa[b]	N/A	31.31	31.55	31.75	31.83	31.98	N/A	
CFS, MPa[b]	N/A	11.57	11.73	11.89	11.94	12.07	N/A	
Mining activity in the closest area[c]	No	No	Large mining	Large mining	Small mining	Large mining	Small mining	

N/A: not available.
[a]Nighttime only.
[b]Stresses were estimated by *Hofmann et al.* [2012].
[c]Mining activity between the PG dike and the GG dike.

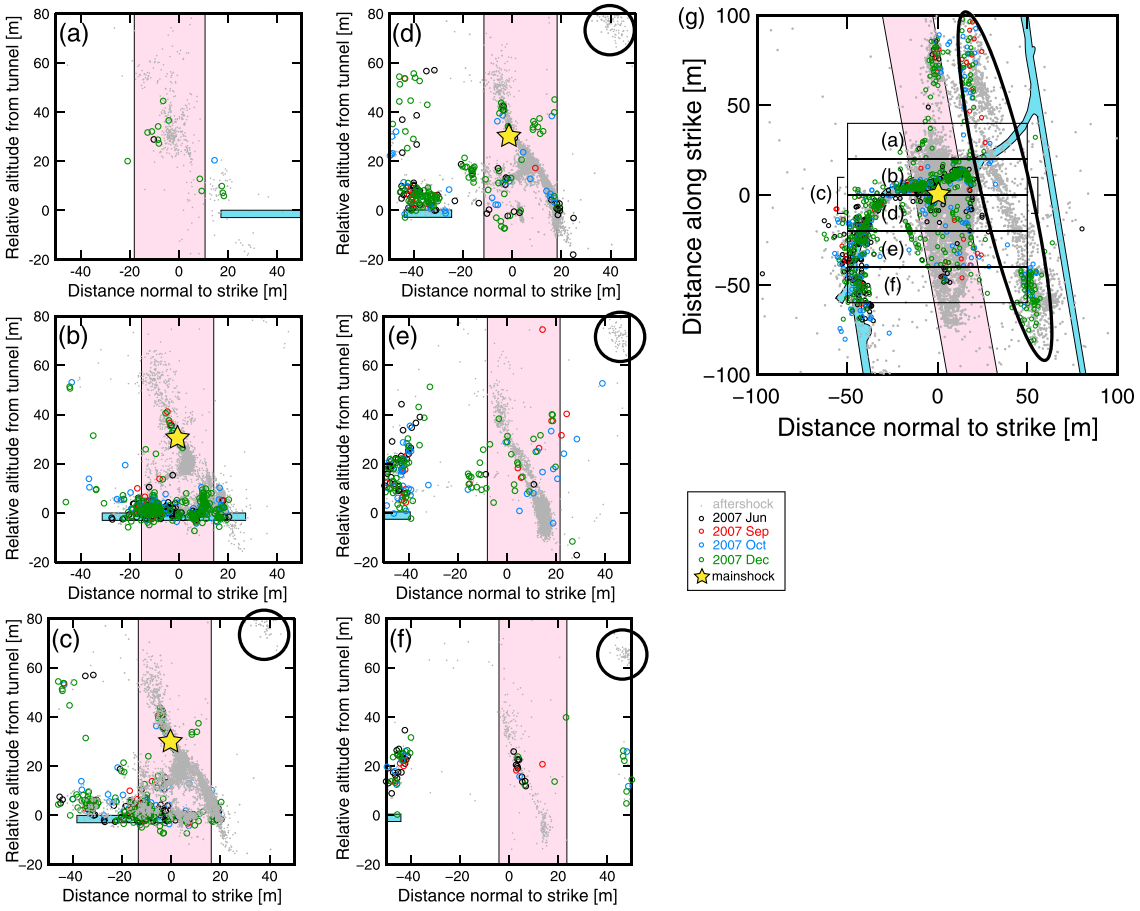

Figure 2. (a–f) Cross sections of the distribution of manually located AE events in each strip in Figure 2g. The time period is from June 2007 to 150 h after the main shock. Light blue and light purple areas indicate the access tunnel and the PG dike, respectively. The AE events after the main shock are indicated by gray dots. Black, red, blue, and green small open circles denote manually picked AE events that occurred in June, September, October, and December, respectively. Yellow star in Figures 2b–2d denotes the main shock hypocenter. The hypocenters of the main shock and AE events after the main shock are from *Naoi et al.* [2011]. The large black circle in Figures 2c–2f and the ellipsoid in Figure 2g enclose AE activity near the active stope edge.

The main minerals in the PG dike were feldspar, clinochlore, magnesiohornblende, and epidote, with minor quartz, calcite, pyrite, titanite, and amphibole. The presence of clinochlore and epidote is indicative of hydrothermal alteration of the dike. Optical microscope images of thin sections of the PG dike are presented in Figures 4c and 4d. Sample 32 (Figure 4c) was collected at a distance of 20 cm from the rupture plane, and sample 33 (Figure 4d) was probably on the rupture plane of main shock. Microscope observations of sample 33 revealed dissolved feldspar and hornblende crystals with sutured grain boundaries, whereas sample 32 showed smoother grain boundaries, indicating that hydrothermal alteration was greater in the vicinity of the rupture plane. In other words, the rupture plane of the main shock was a major conduit for hydrothermal fluids in the PG dike.

The presence of strong XRD peaks corresponding to clinochlore indicates that magnesiohornblende was intensively altered to clinochlore at temperatures higher than 100°C [*Ray et al.*, 2009]. The present-day virgin temperature of the rock mass in the main shock source area is ~60°C, indicating that the time interval of ~1.5 year between the main shock and core recovery was not sufficient to generate the observed intense alteration. Therefore, the hydrothermal activity was not recent but occurred at some point in the geological past, implying that the main shock occurred on a preexisting plane of weakness (discontinuity surface), which acted as a conduit of hydrothermal fluids at some time in the past.

3.2. Spatial Distribution of Foreshocks

Figures 2 and 3 show the cross-sectional and subhorizontal distributions, respectively, of the manually picked, well-located AE events for the six time windows before the main shock (section 2.2 and Table 1)

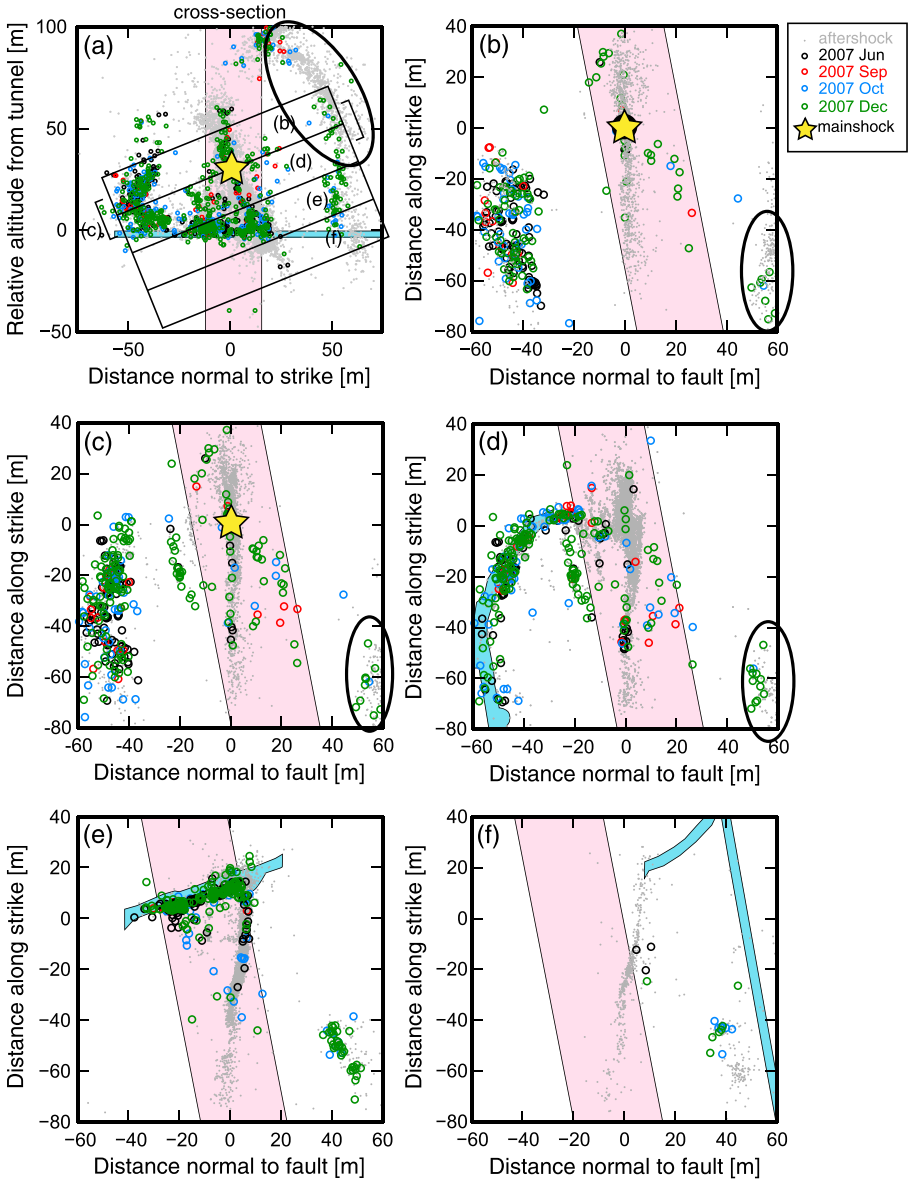

Figure 3. (b–f) Map view of the distribution of AE events in each strip in the section view in Figure 3a. The period is from June 2007 to 150 h after the main shock. Symbols are the same as those in Figure 2.

and within 150 h after the main shock. Either based on manual picks or in situ automatic picks, we define "well-located events" as AE events satisfying all of the following conditions: (1) at least four *P* arrivals are picked, (2) at least four *S* arrivals are picked, (3) the total number of *P* and *S* arrival times is 10 or more; and (4) the root-mean-square residual of arrival times is less than 0.2 ms. The present paper uses only thus defined well-located events.

As noted by *Yabe et al.* [2009] and *Naoi et al.* [2011], AE events after the main shock plotted in Figures 2 and 3 can be divided into three major groups. The first group consists of AE events occurring along the access tunnel. The second group comprises events near the advancing mining face, being 50 m or more away from the rupture plane of the main shock. The third group is composed of aftershocks that delineate the rupture plane of the main shock. All three groups can be recognized in the AE activity before the main shock as well. This is the case in both manually located (Figures 2 and 3) and automatically located (black dots in Figure 5) data sets.

Naoi [2009] fitted a curved surface (aftershock surface) to the sharp planar distribution of aftershocks, thus defining a curved rupture surface of the main shock. Figure 6 shows the frequency distributions of

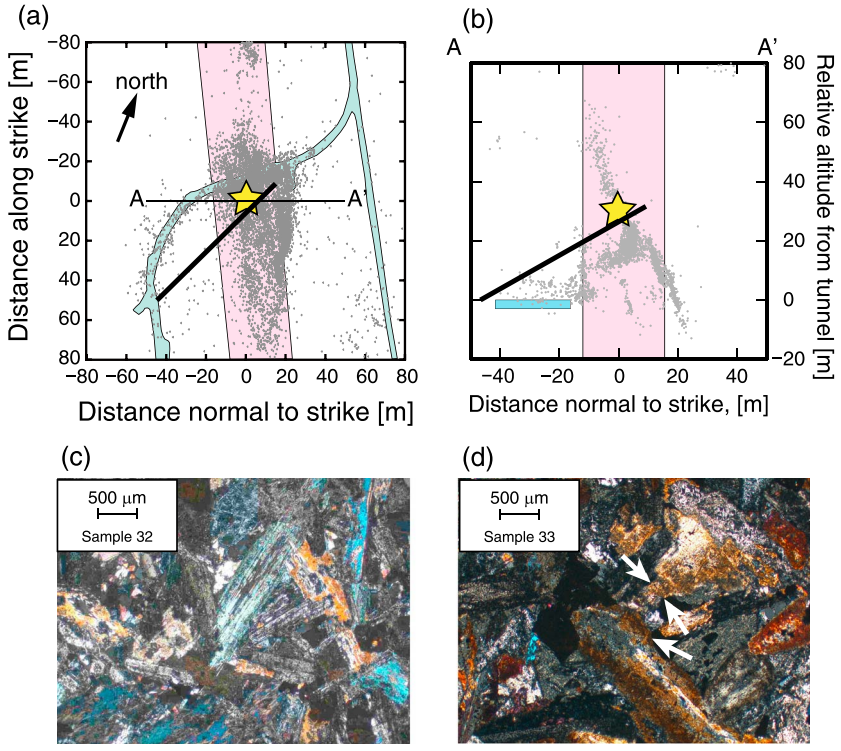

Figure 4. Trace of a borehole drilled after the main shock (thick black line), shown in (a) map view and (b) cross-sectional view along the line A–A′ in Figure 4a; Figure 4b is the same as Figure 2e. Light blue and light purple areas indicate the access tunnel and the PG dike, respectively. The yellow star indicates the hypocenter of the main shock. Gray dots indicate the AE sources that occurred within 150 h after the main shock. The hypocenters of the main shock and AE events after the main shock are from *Naoi et al.* [2011]. (c and d) Optical microscope images of sample 32 and sample 33, respectively (cross-polarized light). White arrows in Figure 4d point dissolved grains of hornblende.

distances from the aftershock surface to the manually located (gray bars) and the automatically located (solid lines) AE sources before the main shock. On the hanging-wall side of the aftershock surface (positive distances), the AE sources are concentrated within 1.2 m of the aftershock surface. The AE sources on the footwall side (negative distances) show a wider distribution, which largely comes from the AE activity in the damaged rock around the access tunnel. To avoid contamination by the AE events related to tunnel damage, the distance distribution of the manually located AE events located 10 m (~3 times the tunnel diameter) or more above the access tunnel (AE events in the box in Figure 5b) is shown by black bars in Figure 6. The data show that AE sources on the footwall side are also concentrated within 1.2 m of the aftershock surface. The width of AE activity concentrated around the aftershock surface is comparable to the location error of the events (~1 m); this shows that the discontinuity surface on which the main shock would later occur had been seismically active already before the main shock.

Figure 7a displays manually located AE events that are within 5 m of the aftershock surface and which occurred during the periods before the main shock and within 150 h following the main shock. The black dashed contour represents the area of significant aftershock activity, as defined by *Naoi et al.* [2011]. As this area can be presumed to represent the rupture area of the main shock, AE events that took place in the aftershock area and within 5 m of the aftershock surface before the main shock are hereafter referred to as foreshocks. Note that this designation of foreshocks is for descriptive purposes only, to refer to on-fault AE events that occurred before the main shock; no causative mechanisms are implied by the word "foreshocks" at this point. Most of the foreshocks distributed in a range of about −50 to 10 m (~60 m span) in the distance along strike and of about −40 to 15 m (~55 m span) in the distance along dip, while the aftershocks were from −70 m to 40 m (~110 m span) in the distance along strike and from −50 m to 35 m (~85 m span) in the distance along dip. The spatial extent of foreshock activity was about half that of aftershock activity.

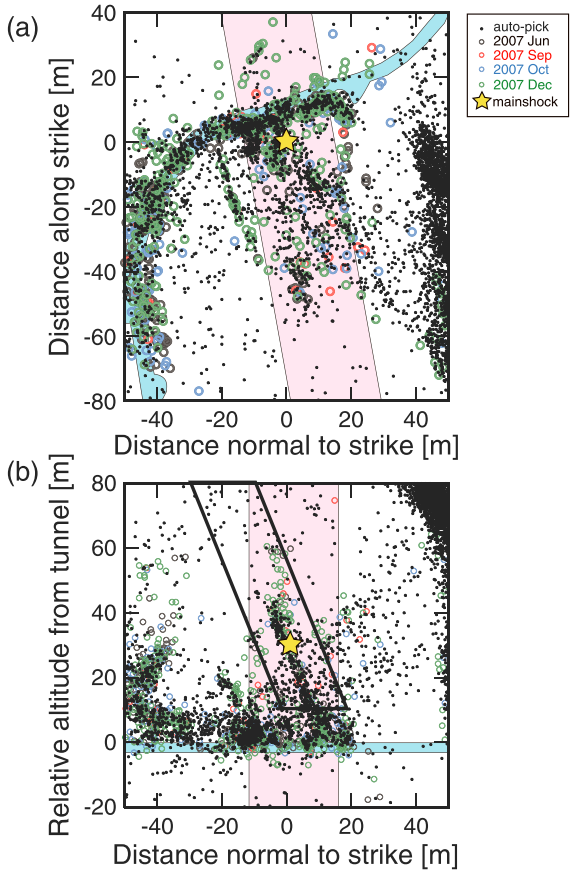

Figure 5. (a) Map view and (b) cross section of distributions of the automatically located hypocenters of AE events before the main shock. The large yellow star indicates the hypocenter of the main shock. Thick black box in Figure 5b encloses the pre–main shock AE events of which distance distributions to the aftershock surface are shown by black bars in Figure 6. Other symbols are the same as Figure 2.

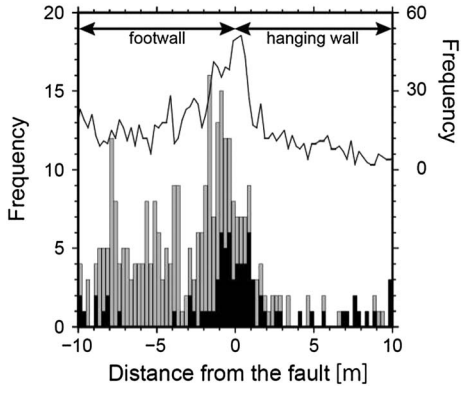

Figure 6. Gray bars indicate the frequency distribution of the distance from the aftershock surface to all of the manually located events that occurred before the main shock, whereas black bars indicate the frequency of events located 10 m or more above the access tunnel. Solid lines show the distance distribution of all of the automatically located events that occurred before the main shock. Left axis is for the manually located events, while right axis for the automatically located events.

The spatial distribution of the areal density of aftershocks (gray contour lines, Figure 7a) indicates the presence of two aftershock clusters, one just below the main shock hypocenter (cluster A1) and one at the bottom edge of the aftershock area (cluster A2), which we defined by density contours whose values are half those of the local maximum.

Although the number of foreshocks plotted in Figure 7a is not sufficient to conclusively compare their spatial distribution with that of the aftershock distribution, the distribution of foreshocks seems to differ from that of the aftershocks. This is more clearly shown in Figure 7b, which displays the distribution of automatically located foreshocks, which are much more numerous than manually located ones. Green contours in Figure 7b represent the areal density of automatically located foreshocks. When we define the extent of clusters by density contours whose values are half those of the local maximum, foreshock clusters F1–F3 bounded by contour lines of 0.4, 0.2, and 0.4 events/m^2, respectively, are clearly recognized (Figure 7b). Another cluster (F4) was identified from a concentration of manually located foreshocks occurring in June (Figure 7a), but this cluster was active only in June. The foreshock clusters (F1–F4) and aftershock clusters (A1 and A2) barely overlap one another.

3.3. Temporal Evolution of Foreshock Activity

It is well known from laboratory experiments that the occurrence rate of AE events significantly increases with time approaching the ultimate failure [*Lei et al.*, 2000; *Thompson et al.*, 2006]. A similar increase in the foreshock occurrence rate has been observed also for some natural earthquakes [*Jones and Molnar*, 1979; *Bufe and Varnes*, 1993; *Yamaoka et al.*, 1999; *Bouchon et al.*, 2013]. On the basis of acceleration in the occurrence rate of foreshocks, *Yamaoka et al.* [1999] succeeded in retrospectively estimating the time of occurrence of an M5.1 earthquake in central Japan. Similarly,

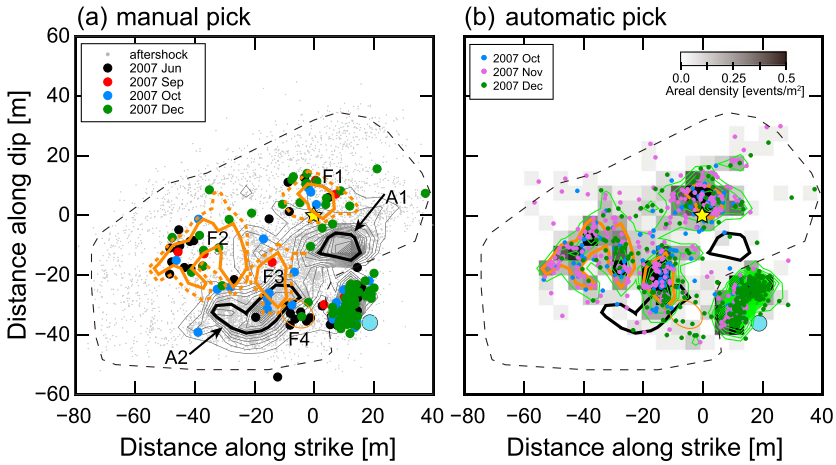

Figure 7. (a) Distribution of the manually located AE events that occurred within 5 m of the aftershock surface during the period from 13 June 2007 to 150 h after the main shock. The hypocenters are projected onto a plane striking N22W and dipping 68° toward east, which approximates the aftershock surface. The yellow star indicates the main shock hypocenter. Black, red, blue, and green solid circles denote the events in June, September, October, and December, respectively. Orange and black thick solid lines enclose the foreshock clusters (F1, F2, and F3) and aftershock clusters (A1 and A2), respectively. Thick orange dashed contours are the expanded area of the foreshock clusters (F1e, F2e, and F3e; see text for details). The thin orange solid contour encloses the foreshock cluster F4. Gray dots denote the aftershocks. Gray contours show the areal density of the aftershocks drawn by feeding areal densities in 5 m × 5 m cells using Generic Mapping Tools [*Wessel and Smith,* 1991] commands of "xyz2grd" and "grdcontour." The contour interval is 1 event/m^2. The thin black dashed contour indicates the aftershock area defined by *Naoi et al.* [2011]. The light blue solid circle is the access tunnel along which the observation network was deployed. (b) Distribution of the automatically located events that occurred before the main shock and within 5 m of the aftershock surface. Their densities in 5 m × 5 m cells are shown by gray scale. Blue, purple, and green solid circles denote events in October, November, and December, respectively. Light green contours show the areal density of the automatically located foreshocks with a contour interval of 0.1 events/m^2.

we examine our data, looking for possible acceleration of foreshock activity. For the simplicity of description, the occurrence time of the main shock is taken as the origin of time *t*, hereafter. That is, 10 days before the main shock, for example, is expressed as $t = -10$ days.

3.3.1. Activity Averaged Over the Whole Foreshock Area

Considering the data recording conditions (see Table 1) and the loading rate history to the observation site, the foreshock activities averaged over the whole foreshock area were examined for three different time spans: 3 months (long term), 17 days (intermediate term), and 65 h (short term) before the main shock. During the long-term period, the automatic in situ picks were obtained continuously from 4 October ($t = -84$ days), except for the data missing period of 11–21 October ($-77 \le t \le -67$ days). During the intermediate-term period, because of the low mining activity around the foreshock area, the source region of the main shock was under a nearly constant stress state. During the short-term period from 21:39 on 24 December to the main shock, waveforms were kept for the all AE events that triggered the observation system. Further, because the mine had been idle since 21 December, no additional loads were applied to the rupture plane of the main shock during the short-term period.

3.3.1.1. Long-Term Activity for 3 Months Before the Main Shock

Figure 8a shows the occurrence rate of the manually located foreshocks in the six time windows of waveform recording (horizontal bars with short vertical bars on both ends), as calculated by dividing the number of all foreshocks by the net duration of the waveform recording in each time window. Temporal variations in the occurrence rate of automatically located foreshocks are also shown in Figure 8a (gray open circles).

The average occurrence rate of the manually located foreshocks during the six time windows was 0.22 ± 0.08 events/h, whereas that of the automatically located foreshocks over the ~3 months was 0.27 ± 0.27 events/h. The slightly higher rate and larger standard deviation of foreshock activity based on the automatic picks are presumably caused by high activity in November, when the manual picking was not available.

Figure 9 shows the mining sequence around our observation site until the occurrence of the main shock. Most of the reef around our site had been mined out before observations commenced in June 2007.

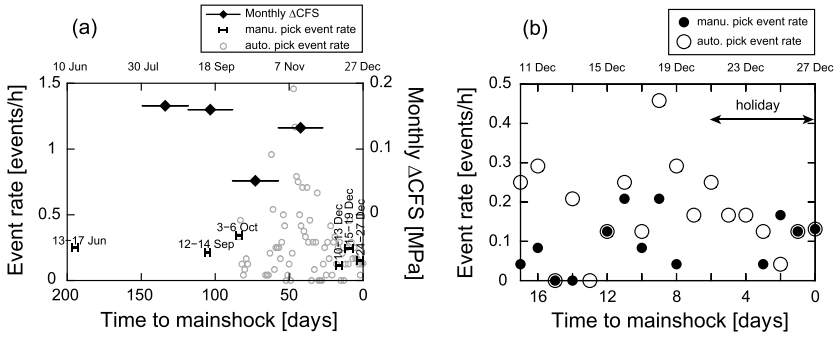

Figure 8. (a) Thick horizontal bars with short vertical bars at both ends show the occurrence rate (left axis) of the manually located foreshocks in the six time windows (see section 2.2 and Table 1) of waveform recording since June 2007, plotted against the time to the main shock. Open circles show the daily occurrence rate (left axis) of the automatically located foreshocks from 4 October 2007 to the occurrence of the main shock. Solid diamonds with horizontal bar show increments of the CFS in each month from the preceding month (right axis). (b) Daily variation in the foreshock occurrence rate during the 17 days leading up to the main shock, plotted against the time to the main shock. Solid and open circles indicate the occurrence rate of the foreshocks located by the manual picks and the automatic picks, respectively.

The reef between the PG dike and the Greater Green (GG) dike was the closest active mining area to our site during the observation period of this study. *Hofmann et al.* [2012] numerically evaluated the mining-induced perturbation of the Coulomb failure stress (CFS) on the rupture plane of the main shock (Table 1 and solid diamond with horizontal bars in Figure 8a). They assumed friction coefficient of 0.37. Their results confirm that mining in a wider area at a smaller distance induces a greater CFS increment. From October to December, when the automatic in situ pick data were obtained almost continuously, mining in the closest active area was most significant during November. Accordingly, *Hofmann et al.* [2012] estimated a larger increment of CFS in November than in October. Though they did not evaluate the stress state in December before the main shock, the smaller area of mining away from the source area of the main shock implies a minor increase in CFS in December before the main shock. *Lei et al.* [2000] demonstrated that AE activity in laboratory experiments shows a positive correlation on the loading rate. *Dieterich* [1994] theoretically showed that the earthquake production rate is proportional to the stressing rate. Therefore, the higher foreshock activity in November likely resulted from the larger increase in CFS associated with active mining. In contrast, the smaller area mined in October and December induced a smaller increase in CFS. As a result,

Figure 9. Map view of the monthly mining sequence from June 2007 to December 2007 around the observation site. Yellow areas were mined out before June 2007, whereas dark gray areas were not mined before 31 December 2007. The yellow star shows the main shock hypocenter. The thick black line encloses the entire aftershock area. Orange areas are the foreshock clusters (F1–F4).

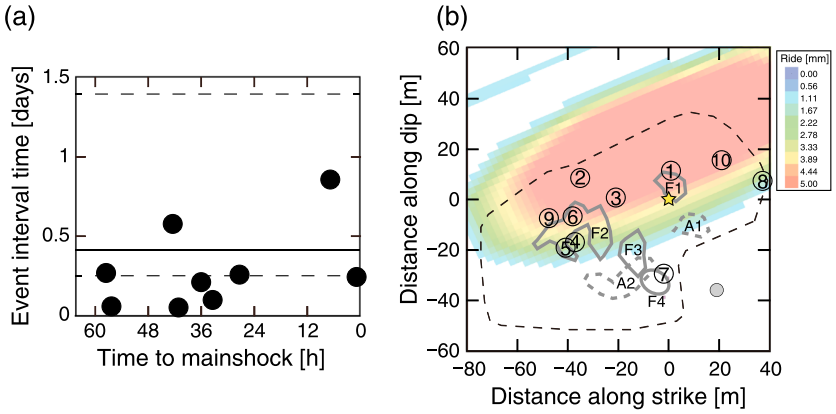

Figure 10. (a) Occurrence intervals of the manually located foreshocks that occurred during the 65 h leading up to the main shock. The interval times are plotted at the occurrence time of the latter event of the two consecutive foreshocks. The solid line indicates the interval time corresponding to the average occurrence rate of the manually located foreshocks during the 17 days leading up to the main shock. The dashed lines indicate the error range estimated for one standard deviation. (b) Spatial evolution of foreshock activity during the 65 h leading up to the main shock projected onto an approximated rupture plane of the main shock, overlaid on the distribution of ride estimated by *Hofmann et al.* [2012]. Numerals in circles are the sequential numbers of each foreshock and are plotted at respective hypocenters. A smaller sequential number is given to the foreshock that occurred later. Thick solid gray contours indicate the foreshock clusters, and thick dashed gray contours indicate the aftershock clusters. A thin dashed line encloses the entire aftershock area. The gray solid circle depicts the access tunnel. The yellow star indicates the main shock hypocenter.

the foreshock activity was lower during these months. Thus, the long-term foreshock activity over several months seems to have been controlled by temporal variations in the loading rate caused by mining activity. Therefore, even if such precursors as acceleration of foreshock activity associated with the preparation process of the main shock had existed, it would have been difficult to distinguish them from the long-term foreshock activity patterns in the present case.

3.3.1.2. Intermediate-Term Activity for 17 Days Before the Main Shock

Figure 8b shows daily variations in the intermediate-term foreshock activity from 10 December, when the waveform storage of the last three time windows was started. On the days (25–27 December) for which the catalogues of manually located and automatically located foreshocks are both available, the foreshock rates from the two data sets agreed well. The average occurrence rate during the 17 days was 0.10 ± 0.07 events/h for the manually located foreshocks and 0.17 ± 0.11 events/h for the automatically located foreshocks. These rates are much lower than the average over the several months before the main shock. This is consistent with the smaller increase in loading during this period. In conclusion, even under an approximately constant stress state, the intermediate-term activity of foreshocks over the entire area of the forthcoming main shock rupture did not show any precursory behavior, such as acceleration in the foreshock rate with time approaching the main shock.

3.3.1.3. Short-Term Activity for 65 h Before the Main Shock

To further examine the foreshock activity over a further shorter period, we examined foreshock activity for 65 h after 21:39 on 24 December. Because the mine had been idle since 21 December, the seismic noise level during this time was relatively low, and hence, our network was performing at its best in terms of event detectability.

We were able to detect 10 foreshocks by the manual picking, whereas only seven of these events were detected by the automatic in situ picking. Because of the small number of foreshocks, it was not practical to evaluate the foreshock activity by their occurrence rate. We used the interval times between consecutive foreshocks to evaluate temporal variation in the foreshock activity with a higher time resolution. Figure 10a shows temporal variations in the interval time of the manually located foreshocks. Most of the foreshock interval times during the period of $-65\ \text{h} \le t \le -27\ \text{h}$ were less than 0.42 days, which is the interval time corresponding to the average occurrence rate over the intermediate-term period (0.10 events/h). Therefore, the foreshock activity during this period was apparently higher than that during the intermediate-term period. However, a quiet period of ~20 h followed this period of apparently high foreshock activity. As a result, the average interval time in the short-term period was 0.29 days, which is shorter than the interval time expected from the average occurrence rate for the intermediate-term period. Considering that the

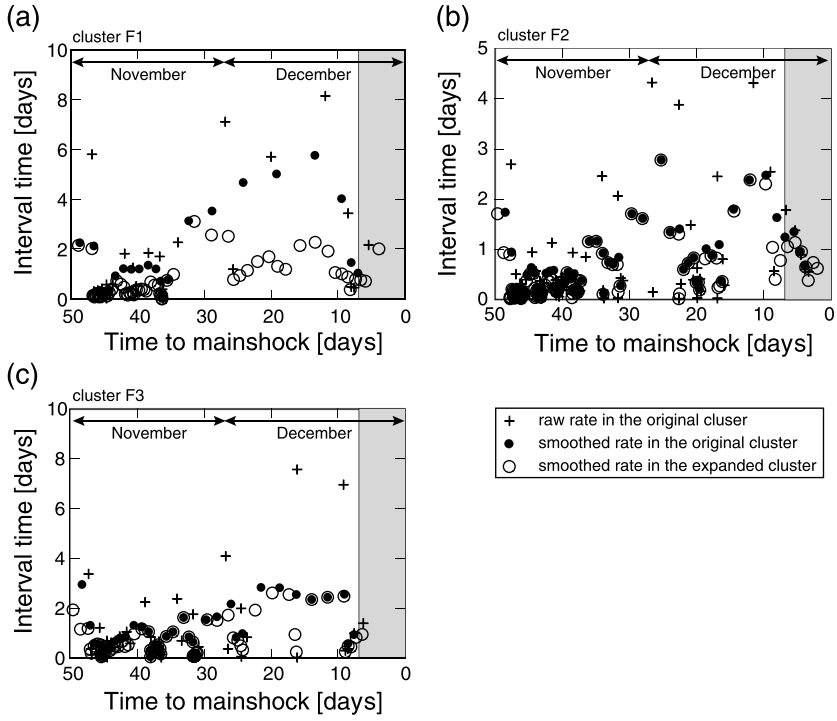

Figure 11. Occurrence intervals between the automatically located foreshocks in (a) F1, (b) F2, and (c) F3 during the 50 days leading up to the main shock. Crosses are raw data plotted at the occurrence time of the latter event of the two consecutive foreshocks. Solid and open circles show the moving average of interval times in the original (F1–F3) and the expanded versions (F1e–F3e) of the clusters, respectively, with a window length of three data points and a shift of one. The shaded area indicates the mine's holiday.

lower noise level during the holiday should improve the detectability of the network, it is difficult to conclude that the rate of the short-term foreshock activity just before the main shock increased as expected from accelerating expansion of a preslip patch.

Figure 10b shows the spatial evolution of the 10 foreshocks that occurred during the 65 h leading up to the main shock and a slip (ride) distribution required to release the CFS estimated by *Hofmann et al.* [2012]. Foreshock clusters F1 and F2 were located in the expected slip area, while F3 was on its margin. Among the 10 foreshocks that occurred during the last 65 h leading up to the main shock, four foreshocks (#9 and #6–4) occurred in and around F2. The foreshocks #3 and #2 occurred in the high CFS zone between F2 and F1, and foreshock #1 took place just beside F1. This temporal variation of foreshock locations suggests that they migrated in the direction from F2 to F1 along the high CFS area in general, though the migration was not really straightforward. The CFS seems to be highest near F1. Three of the six interval times shorter than the average during the intermediate term were observed for the foreshocks in and around cluster F2. This will be further discussed in detail later (section 4.3).

3.3.2. Activity in Each Foreshock Cluster

3.3.2.1. Long-Term Activity in Each Foreshock Cluster

Ohnaka and Kuwahara [1990] pointed out that the preparation process will comprise phases II (quasistatic steady growth) and III (stable but accelerating growth up to a critical patch length) alone, when there is a weak patch which plays the role of slip nucleus. As discussed later (section 4.3), the foreshock clusters seem to occur in weak patches that played the role of slip nuclei. Therefore, spatial and temporal evolution of the foreshock activities in individual clusters may be interpreted to indicate evolution of the preparation process (phase II or III) at multiple sites. We evaluate the foreshock activity in individual clusters in this section.

Figure 11 shows temporal variations in activities of the automatically located foreshocks in F1–F3 during the 50 days leading up to the main shock. Because the number of foreshocks in each cluster was not large, the activity was evaluated by interval times between consecutive foreshocks. Because the activity in F4 was

mostly limited to June, it was excluded from the investigation. Interval times naturally fluctuate due to small scale heterogeneities within each cluster, besides a possible systematic evolution coherent over the cluster size such as a preslip patch. Therefore, we took the running average (solid circles) of the interval times to reduce scattering. Considering the trade-off between reduction of the scattering and degradation of time resolution, the averaging window length was set to three data points. Further, to see how the definition of the spatial extent of the clusters affects the result, we tried the same analysis by redefining F1 and F3 at the contour of a lower density of 0.2 events/m^2, which defines expanded versions of clusters F1e and F3e (Figure 7a). Because the original version of F2 was already defined by the contour line of 0.2 events/m^2, its expanded version (F2e) was defined by the contour of 0.1 events/m^2. However, the contour of 0.1 events/m^2 encloses the F1 and F3, too. Hence, to define F2e, truncation to the right was applied at a line between F2 and F3. The boundaries of the expanded version of the foreshock clusters are drawn by thick orange dashed lines in Figure 7a. Open circles in Figure 11 show the results of three-point running average for the expanded clusters F1e–F3e.

The interval times in F1–F3 were relatively short in November because of the faster progress of mining in this month. The interval time in F1 (solid circles in Figure 11a) gradually increased starting at $t \sim -30$ days. Then, the interval times decreased starting about $t \sim -10$ days, but the activity ceased, when the holiday began on 21 December. Because more foreshocks were included in F1e, the interval times (open circles in Figure 11a) were much shorter than those in the original definition. However, the temporal variation after $t \sim -28$ days generally showed a similar pattern. Except for foreshock #1 that occurred just outside F1, in Figure 10b, no foreshocks occurred for the 5.4 days before the main shock in either F1 or F1e.

For -24 days $\lesssim t \lesssim -9$ days, the foreshocks in F3 occurred at a nearly constant interval of 2.6 ± 0.2 days (solid circles in Figure 11c), being much lower activity than that in November (0.4–0.5 days for $t < -30$ days). The activity became as high as that in November for a few days (-9 days $\lesssim t \lesssim -8$ days), but it ceased when the holiday began. These characteristics were recognized also in F3e (open circles in Figure 11c). Shorter interval times at $t \sim -16$ days were caused by an activity to the left (farther from the main shock hypocenter) of F3.

Activity in F2 once became lower at the beginning of December (Figure 10b). Then, it became as high as in November for ~7 days (-22 days $\lesssim t \lesssim -16$ days) and lowered again. The interval time in F2 started to decrease linearly from about 10 days before the main shock ($t \sim -10$ days); in other words, the activity in F2 accelerated in inverse proportion to the time to the main shock, as observed for some natural earthquakes [*Jones and Molnar*, 1979; *Bufe and Varnes*, 1993; *Yamaoka et al.,* 1999]. This acceleration continued even after the holiday started. The activity in F2e until 10 days before the main shock ($t \lesssim -10$ days) was generally identical to that in F2. Shorter interval times in F2e than in F2 at -9 days $\lesssim t \lesssim -7$ days was caused by the occurrences of two foreshocks just above F2, where a higher CFS is expected (Figure 10b). The activity in F2e also showed the acceleration with time to the main shock after $t \sim -7$ days.

To further confirm robustness of the abovementioned evolution of the foreshock activity in each cluster, we recalculated the density contour by using 5 m × 5 m cells shifted by 2.5 m in both along-strike and along-dip directions. Clusters F1s, F2s, and F3s were defined by recalculated contour lines of 0.4, 0.2, and 0.4 events/m^2, respectively. The foreshock activities in individual clusters were almost identical to those in the corresponding original clusters (F1, F2, and F3).

A similar decrease in the interval time to that observed for the 10 days before the main shock in F2 is also seen, for example, for -35 days $\lesssim t \lesssim -30$ days in F2, and for -40 days $\lesssim t \lesssim -36$ days in F1 and F3. However, these temporary activations of foreshock clusters occurred during a period of active mining. Also, the raw data (pluses in Figure 11) in these periods show larger scattering around the running average, compared with the raw data for the 10 days before the main shock in F2. Therefore, these apparent accelerations could be caused by spatial and temporal variations in stress perturbation induced by mining activity, in contrast to the acceleration in F2 just before the main shock that occurred under a quasi-constant stress state.

3.3.2.2. Foreshock Activity in Cluster F2 for 7 Days Before the Main Shock

Figure 12a shows the occurrence times of the foreshocks in clusters F2, F2e, and F2s in the holiday period (-7 days $\lesssim t \lesssim 0$ days), during which there was no mining activity. The occurrence times of the manually located foreshocks in Figure 10 are also shown. In F2, five automatically located foreshocks and two manually located foreshocks (the foreshocks #6 and #5 in Figure 10) occurred during this period. Cluster F2e includes three more foreshocks, all of which were located by automatic picks. However, the net

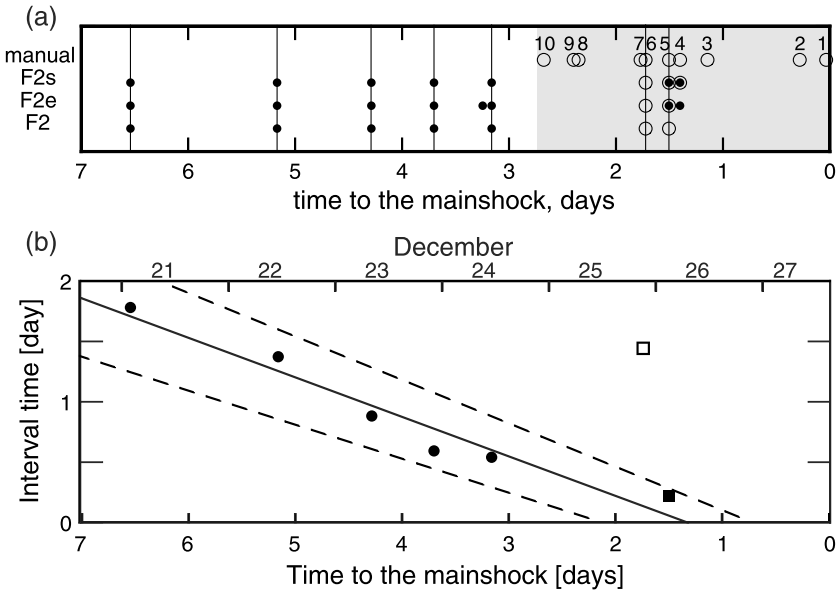

Figure 12. (a) Occurrence times of the manually located (open circles) and the automatically located (solid circles) foreshocks in (second row) clusters F2, (third row) F2e, and (fourth row) F2s during the 7 days before the main shock (holiday period). Open circles in top row show occurrence times of all the manually located foreshocks in this period. Numerals attached to the manually located foreshock are the event number shown in Figure 10b. Vertical lines indicate the occurrence times of the foreshocks in F2. (b) Occurrence intervals between the automatically located foreshocks (solid circles) and the manually located foreshocks (between foreshocks #6 and #5, solid square) in F2 during the 7 days leading up to the main shock, as well as the interval time between the last automatically located foreshock and foreshock #6 (open square), which was the first of manually located foreshocks in F2 in this period. Solid line represents the linear decreasing best fit trend for the unified interval time data set of the automatically (solid circles) and the manually located (solid square) foreshocks, except for the interval time between the last automatically located foreshock and foreshock #6 (open square). Dashed lines indicate the error range of the fitting.

increase in the foreshock activity in F2e comparing with F2 is two, because one of the three is actually foreshock #5. One of the two net additions is foreshock #4, whose manually located hypocenter is outside of F2e. In the area of F2s, the manually located and the automatically located hypocenters of the foreshock #4 are included in addition to the foreshocks in F2. The automatically located hypocenter of foreshock #5 is also included, though its manually located hypocenter was already included in the F2. The net increase in the foreshocks in F2s from the F2 is only one, which is foreshock #4.

Temporal evolution of the interval time in F2 is shown in Figure 12b. The five interval times between consecutive automatically located foreshocks (solid circles in Figure 12b), an interval time between the two manually located foreshocks (solid square in Figure 12b), and the interval time between the last automatically located foreshock and foreshock #6 (open square) are shown in this figure. The first interval time of the automatically located foreshock was calculated from the occurrence time of the foreshock that occurred just before the mining activity halted and the first foreshock in the holiday. There is a time gap of 10.3 h between the occurrence of the last automatically located foreshock and the time when the waveform storage was enabled. The interval time prior to foreshock #6 (open square) is less reliable, because it is possible that some of the foreshocks that occurred during the time gap might be located in cluster F2, if we had waveforms for manual location.

The six interval times, except for the less reliable one (open square in Figure 12b), show a monotonic and almost linear decrease with time to the main shock under the constant stress state for at least 7 days before the main shock. However, when the interval time prior to foreshock #6 is included, this linear decreasing trend in the interval time becomes less clear. This will be evaluated in detail later (section 4.1).

4. Discussion

It is inferred from the mining sequence that the loading rate to the rupture plane of the main shock was very low during the month leading up to the main shock. The stress state was constant especially during the last 7 days prior to the main shock, as this was a mining holiday. This suggests that the main shock could have been

the static fatigue or the ultimate failure that was self-driven under a constant load. It is known from laboratory experiments that an acceleration of deformation, called tertiary creep, is associated with the static fatigue. Tertiary creep involves localized deformation along a plane, on which the ultimate failure nucleates [e.g., *Kurita et al.,* 1983]. Therefore, tertiary creep should correspond to phase III (stable but accelerating growth of preslip patch with the increasing stress intensity factor) of the preparation process of dynamic instability defined by *Ohnaka and Kuwahara* [1990]. The AE events associated with tertiary creep are also concentrated on the plane of localized deformation in laboratory [e.g., *Satoh et al.,* 1996; *Yanagidani et al.,* 1985], and their occurrence rate increases rapidly as the creep accelerates [e.g., *Lockner and Byerlee*, 1977; *Nishizawa et al.,* 1985; *Yanagidani et al.,* 1985]. *Jouinaux et al.* [2001], *Lei* [2003], and *Lei et al.* [2003, 2004] performed triaxial compression tests to demonstrate that the deformation and AE sources associated with tertiary creep are localized along the plane of weakness that will be faulted upon the ultimate failure, even when the rock sample contains a preexisting macroscopic plane of weakness (a healed joint). In this section, we discuss how the foreshock activity observed in the present paper can be understood on the basis of such laboratory knowledge.

4.1. Reliability of Immediate Foreshock Acceleration in Cluster F2

The AE events prior to the main shock were concentrated on a preexisting weakness on which the main shock would later take place. This implies that tertiary creep had started in the source region [e.g., *Lei et al.,* 2003]. However, a precursory anomaly, such as acceleration of foreshock occurrence, was not recognized when the foreshock activity over the entire area was analyzed. This suggests that the weak surface in the foreshock area as a whole had not reached a critical state (i.e., stress levels approaching the strength of the formation) to allow for the initiation of self-driven tertiary creep.

The foreshocks were concentrated in four clusters so that deformation was heterogeneously distributed over the preexisting plane of weakness, meaning in turn that the quasistatic steady growth of preslip patch occurred at multiple sites [*Lockner*, 1993; *Thompson et al.,* 2005]. The temporal variations in the foreshock activity within individual clusters should reflect temporal variations in the quasistatic growth of preslip patch at each site. The quasistatic nucleus at F4, which was out of the CFS concentration area (Figure 9b), halted long before the main shock. The activity in F1 and F3, which were among the three clusters that remained active until December, became higher from 10 days before the main shock, despite the low stressing rate, but the activity ceased when the stress increment was completely stopped for the mine's holiday. This implies that the quasistatic growth of the preslip patch at these sites (F1 and F3) was near the transition from the steady growth to the accelerating growth.

The foreshock interval time in cluster F2 showed a monotonic, linear decrease with time to the main shock even after the additional loading ceased at $t = -7$ days, when the less reliable datum is excluded. However, because the number of interval time data is small, it is possible that the observed monotonic, linear decrease in interval time occurred by chance. Therefore, we evaluate the probability for the linear decrease in interval time to occur by chance to the observed extent of clarity. We randomly generated $N+1$ interval times Δt_i ($i = 0, N$) that obey the Poisson distribution with an average interval time T. Then, the occurrence time t_i ($i = 1, N$) of N foreshocks was calculated by summing up interval times $\left(t_i = \sum_{j=0}^{i-1} \Delta t_j\right)$. Finally, a line was fitted to the synthetic relation between t_i and Δt_i. Correlation coefficient r between the synthetic data and the best fit line was also calculated. By repeating this procedure by 100,000 times for specific values of N and T, we evaluated the probability p of the by-chance occurrence of the monotonic, linear decrease in the interval time with the time to the main shock with $r \geq r_c$, where r_c is a reference value.

According to the average of interval times for $t \geq -50$ days, we set $T = 14$ h, though the probability p was insensitive to T for the tested range of $1 < T < 35$ h. When the less reliable interval time prior to foreshock #6 (open square in Figure 12b) was ignored, $N = 6$ and $r \sim 0.97$. Then, we set $N = 6$ and $r_c = 0.97$, and obtained p ~0.07%. Even when the condition was relaxed to $N = 5$ and $r_c = 0.9$, p ~1.8%. However, when the interval time before foreshock #6 was included, N was increased to 7 but r was degraded to 0.61. By using $N = 7$ and $r_c = 0.61$, p ~6%. In cases of F2e and F2s, $(N, r) = (9, 0.51)$ and $(8, 0.54)$, respectively, when the interval time before foreshock #6 was included. By setting $r_c = r$, the probabilities for these cases were also p ~6–7%. Therefore, the observed monotonic, linear decrease in the interval time of the foreshocks with respect to the time to the main shock is statistically significant with a significance level better than

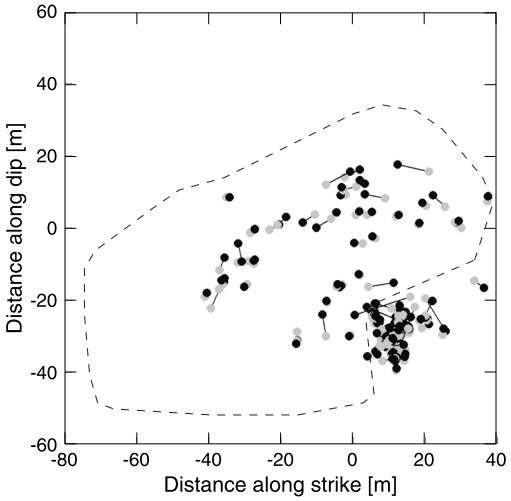

Figure 13. Comparison between the hypocenters of the pre–main shock events located by using the automatically picked (black solid circles) and the manually picked (gray solid circles) arrival times. Hypocenters of the same foreshock are connected by a line. The hypocenters are projected onto a plane with strike of N22W and dip of 68° that approximate the aftershock surface. Dashed contour indicates the aftershock area defined by *Naoi et al.* [2011].

98%, if the less reliable interval time is ignored. When the less reliable interval time before foreshock #6 is included, the significance level is ~93%.

4.2. Reliability of the Main Shock Hypocenter Relative to the Foreshock Clusters

If the preparation process proceeds on a uniform fault, it is expected that the main shock rupture would initiate from an edge of the immediate foreshock area [e.g., *Ohnaka*, 1992]. The main shock hypocenter in the present paper was located at the edge of F1, whereas the acceleration of immediate foreshock activity occurred at F2 (Figure 10b). The main shock hypocenter was located relative to the manually located aftershocks [*Naoi et al.,* 2011]. An error in the hypocenter of the main shock was estimated to be several meters, being much smaller than distance of ~30 m between the main shock hypocenter and F2. The separation between the main shock hypocenter and F2 is not apparent due to the location error of the main shock.

On the other hand, we defined the foreshock clusters according to distribution of the foreshocks located by using the automatic in situ picks, while the main shock hypocenter was located relative to the manually located aftershocks [*Naoi et al.,* 2011]. It is concerned that hypocenters located by the automatic picks and by the manual picks may systematically shift from each other. Especially, because our observation network had a rather one-dimensional configuration along the access tunnel that was subnormal to the aftershock plane, a slight difference between the automatically picked arrival times and the manually picked arrival times could result in a significant shift of the transverse coordinate of the hypocenter location around the tunnel. Therefore, it is possible that this transverse shift caused the apparent separation between the main shock hypocenter and F2. To see how the hypocenter location would depend on the arrival time data set, Figure 13 shows hypocenter pairs (the automatically located vs. the manually located) of 153 events before the main shock satisfying the following two conditions: (1) both of the hypocenters well located by using the automatic picks and by using the manual picks were within 20 m from the aftershock surface, and (2) at least one of the two hypocenters was within 5 m from the aftershock surface. Distances between the automatically located hypocenters (black circles) and the manually located hypocenters (gray circles) were as small as 2.6 ± 2.5 m on average, being comparative to the location error based on the manually picked arrival times. Not only the average distance but the maximum distance of ~10 m between the automatically located and the manually located hypocenters was also much smaller than the distance between the main shock hypocenter and F2. Rotational shifts of hypocenters around the access tunnel were dominant for all events, as expected from the array configuration. Some events show clockwise rotations from the automatically located to the manually located hypocenters, but others counterclockwise. That is, the rotational shifts were not unidirectional. Further, distances between the manually located and the automatically located hypocenters were independent of the distance from the observation network. Therefore, there should be no systematic error in relative location between the manually located and the automatically located foreshock distributions. So, we have to accept the observation that the main shock initiated somewhat away from F2, where the immediate acceleration of foreshock activity occurred.

4.3. Possible Scenarios of Preparation Process Immediately Before the Main Shock

Stick-slip experiments by *Thompson et al.* [2005] and *McLaskey and Lockner* [2014] showed that the ultimate slip events breaking the entire fault sometimes initiated just beside an immediate foreshock cluster but sometimes

started at a point away from the immediate foreshocks. Both cases were observed in a series of stick-slip events in a single experiment, suggesting that the preparation process of the ultimate event is sensitive to heterogeneities of stress and/or strength. The sensitivity of the preparation process to the heterogeneous distribution of stress and strength is also demonstrated by a numerical simulation [*Noda et al.,* 2013].

We have shown that the quasistatic preparation of the main shock in the present paper occurred at multiple sites on the rupture plane of the forthcoming main shock (the foreshock clusters). The foreshock cluster F2 showed the acceleration for the 7 days before the main shock, suggesting the beginning of self-driven quasistatic growth of the preslip patch at F2. However, the main shock initiated from a point away from F2 but close to F1. This may imply that some interaction between the preslip patches played an important role in the final stage of the preparation process of the main shock. Below, we discuss two possible scenarios of the interaction that might be involved in the preparation process for the 7 days before the main shock. The significant difference between the two scenarios is the role of foreshock #1. In the first scenario, the occurrence of foreshock #1 causes clock advance of the occurrence of the main shock. In the second one, the immediate foreshocks including foreshock #1 are regarded merely as an indicator of the propagating stress concentration ahead of the growing patch (F2), and the occurrence of foreshock #1, in itself, does not contribute to the preparation process of the main shock.

Due to the limited amount of the data, it is difficult to conclude which of the abovementioned scenarios was the case. Further, there may be other possible scenarios. The important fact to be kept in mind for making any scenario is that the external load was constant for the 7 days leading up to the main shock thanks to the mine's holiday. Also, it is important to note that locations of individual clusters were persistent for at least 3 months in spite of the significant changes in geometry of mining area that controlled the spatial pattern of stress perturbation, implying that the spatial pattern of foreshock activity was most likely controlled by the heterogeneity of strength on the preexisting plane of weakness to be ruptured by the main shock. That is, the foreshock clusters represented weak patches surrounded by higher background strength. The accelerating foreshock activity in F2 suggests self-driven growth of the preslip patch at F2. Therefore, the stress concentration ahead of the growing preslip patch at F2 should be the only driving force to promote the preparation processes under the constant external load.

4.3.1. Scenario 1: Delayed Cascade-Up by Foreshock #1

The extent of F1 was comparable to the critical size (~15 m) [*Ohnaka*, 2004] of the preslip patch of an M~2 earthquake on a homogeneous fault. The last foreshock (foreshock #1 in Figure 10b) occurred at the edge of F1 and within 10 m from the main shock hypocenter, which is much shorter than the distance between the main shock hypocenter and F2. It is, then, possible that the main shock was triggered by the stress perturbation associated with the occurrence of foreshock #1. The duration of the dynamic nucleation of an M~2 earthquake is expected to be shorter than 1 min [*Ohnaka and Shen*, 1999]. However, the main shock took place ~50 min after the occurrence of foreshock #1. Therefore, the stress perturbation by foreshock #1 is unlikely to have directly triggered the main shock. Some slower aseismic processes such as the delayed cascade-up [*Noda et al.,* 2013] may have been involved. That is, afterslip of foreshock #1 might have mildly accelerated the quasistatic nucleation in F1 and, some times later, the preslip patch became critical. In this case, the preslip patch at F2 did not directly contribute to the occurrence of the main shock.

However, we still would like to point out a possibility that F2 indirectly affected the timing of the main shock occurrence. No foreshock activity in F1 for the 7 days before the main shock until foreshock #1 (Figure 11a) suggests that the preparation process in F1 had halted or significantly slowed down, since additional loading due to mining activity was stopped. To regain the preslip patch at F1, a loading mechanism other than mining activity is required. The growing preslip patch at F2 induced a significant stress concentration around it. This stress concentration in addition to the higher CFS between F2 and F1 might generate foreshocks #3 and #2 and also reactivated the preslip patch at F1. In this sense, the accelerating growth of the preslip patch at F2 might have been indirectly involved in determining the occurrence time of the main shock.

4.3.2. Scenario 2: Coalescence of F2 and F1

Cluster F2 was the largest among the foreshock clusters (F1–F3) that were active until December. Because the stress concentration around a preslip patch, which drives the growth of the preslip patch, is higher for a larger patch, the largest cluster F2 should have been the one closest to the critical state. The accelerated foreshock activity in F2 from $t = -7$ days or earlier (Figure 12) also indicates that the preslip patch at F2 might have evolved to stable but accelerating growth (phase III). The linear extrapolation of the observed interval

times predicts that the preslip patch at F2 grew up to the critical patch length expected of the low strength in F2 at –2.1 days $< t <$ –0.7 days. However, F2 did not proceed to the dynamic instability, which we tend to ascribe to some strength barrier (higher background strength) around the F2. Then, the occurrence of foreshocks #3 and #2 suggests that the preslip patch expanded from F2 in the direction of F1 along the high CFS zone (Figure 10b), at a lower velocity once retrograded to the quasistatic steady growth, which might be sustained by the higher CFS between F2 and F1. When the expanding slip patch passed through the strength barrier, it coalesced with the small preslip patch at F1 and grew in a stepwise manner. The coalesced slip patch (F1 + F2) might induce enough stress concentration to cause the dynamic instability even outside the high CFS zone. Then, the main shock would initiate from an edge of F1 + F2 patch. Thus, such an on-fault strength barrier between F2 and F1 can explain both of the initiation of the main shock away from the immediate foreshock acceleration site (F2, Figure 10b) and the delayed occurrence of the main shock (Figure 12).

5. Conclusions

An observation network consisting of high-frequency AE sensors was deployed to monitor microfracturing in a dike (the PG dike) in a deep gold mine in South Africa. An earthquake of Mw 2.2 occurred in the dike on 27 December 2007, 6 months after the installation of the network.

A borehole passing through the source region and intersecting the rupture plane of the main shock was drilled ~1.5 years after the occurrence of the main shock. Rock samples collected from the borehole show evidence of an ancient hydrothermal activity localized along the rupture plane, indicating that the main shock ruptured a preexisting plane of weakness.

The AE activity during the 6 months prior to the main shock delineated the rupture plane in advance of the main shock. The rupture plane of the main shock, as estimated from the aftershock distribution, has experienced degradation over about half of its extent, as indicated by the wide distribution of foreshocks. Long-term variations in the foreshock activity are well explained by temporal variations in the stressing state in the source region of the main shock due to nearby mining. Foreshock activity as a whole did not show acceleration precursory to the main shock that is usually observed in laboratory experiments.

Throughout the study period, the foreshocks tended to concentrate in four clusters, although one of them died out long before the main shock. The three clusters that remained active until December (F1–F3) could be sites of localized quasistatic nucleation (preslip) patches. Long-term stationarity of cluster locations in spite of the time-varying geometry of nearby mining suggests that the foreshock patches represented relatively weak portions of the existing plane of weakness. The largest clusters (F2), which should induce a higher stress concentration around it than the other clusters, showed clear acceleration of its activity during at least 7 days leading up to the main shock under the constant external load, suggesting the transition from quasistatic growth to accelerating growth of the preslip patch at F2. However, the main shock initiated at a point close to F1, away from F2. This might be explained by considering an interaction between the slip patches at F1 and F2 through the stress concentration ahead of the expanding preslip patch at F2, which should be the only driving force of the preparation process of the main shock under the constant external load.

Although the heterogeneity of geological structures obscures the straightforward manifestation of the preparation process of the ultimate failure, the present thorough analysis suggests that the essence of such quasistatic nucleation, as known from the fracture mechanics and laboratory experiments, was probably recorded in the pre-M2 AE data on a natural discontinuity surface at a depth of 3.3 km.

Acknowledgments

Technical supports from the Mponeng Gold Mine (AngloGold Ashanti), Seismogen Cc, Kapenta Mining Cc, Institute of Mine Seismology, Lourina Coetzee, and the Council for Scientific and Industrial Research are greatly appreciated. Critical and constructive comments by T. Hori, an associate editor and an anonymous reviewer, were useful to improve the manuscript. Discussion with G. Hofmann deepened our understanding on stress state before the main shock. We dedicate this paper to the late Gilbert Morema, who was the real engine of the AE observation. This work was partly supported by Grants-in-Aid for Scientific Research (A-18253003, A-14204040, B-18403007, A-21246134, 07J09904, and S-21224012), the Science and Technology Research Partnership for Sustainable Development (SATREPS), a joint research program of the Earthquake Research Institute, the 21st Century COE Program of Tohoku University, and the Observation and Research Program for the Prediction of Earthquakes and Volcanic Eruptions of the Ministry of Education, Culture, Sports, Science and Technology (MEXT) of Japan. Data used in this paper are available from the corresponding author.

References

Bouchon, M., V. Durand, D. Marsan, H. Karabulut, and J. Schmittbuhl (2013), The long precursory phase of most large interplate earthquakes, *Nat. Geosci.*, *6*, 299–302, doi:10.1038/ngeo1770.

Bufe, C. G., and D. J. Varnes (1993), Predictive modeling of the seismic cycle of the Greater San Francisco Bay Region, *J. Geophys. Res.*, *98*, 9871–9883, doi:10.1029/93JB00357.

Chamber of Mines Research Organization (COMRO) (1988), *An Industry Guide to Methods of Ameliorating the Hazards of Rockfalls and Rockbursts*, Chamber of Mines of South Africa, Johannesburg.

Chester, F. M., J. P. Evans, and R. L. Biegel (1993), Internal structure and weakening mechanism of the San Andreas fault, *J. Geophys. Res.*, *98*, 771–786, doi:10.1029/92JB01866.

Dieterich, J. (1992), Earthquake nucleation on faults with rate- and state-dependent strength, *Tectonophysics*, *211*, 115–134.

Dieterich, J. (1994), A constitutive law for rate of earthquake production and its application to earthquake clustering, *J. Geophys. Res.*, *99*, 2601–2618, doi:10.1029/93JB02581.

Dodge, D. A., G. C. Beroza, and W. L. Ellsworth (1995), Foreshock sequence of the 1992 Landers, California, earthquake and its implications for earthquake nucleation, *J. Geophys. Res.*, *100*, 9865–9880, doi:10.1029/95JB00871.

Dodge, D. A., G. C. Beroza, and W. L. Ellsworth (1996), Detailed observations of California foreshock sequences: Implications for the earthquake initiation process, *J. Geophys. Res.*, *101*, 22,371–22,392, doi:10.1029/96JB02269.

Ellsworth, W. L., and G. C. Beroza (1995), Seismic evidence for an earthquake nucleation phase, *Science*, *268*, 851–855, doi:10.1126/science.268.5212.851.

Hauksson, E. (2010), Spatial separation of large earthquakes, aftershocks, and background seismicity: Analysis of interseismic and coseismic seismicity patterns in southern California, *Pure Appl. Geophys.*, *167*, 979–997, doi:10.1007/s00024-010-0083-3.

Hofmann, G., H. Ogasawara, T. Katsura, and D. Roberts (2012), An attempt to constrain the stress and strength of a dyke that accommodated a ML2.1 seismic event, in *Proceedings of the Second Southern Hemisphere International Rock Mechanics Symposium, Southern African Institute of Mining and Metallurgy, 16 May 2012, Sun City, South Africa*, pp. 436–450, Southern African Institute of Mining and Metallurgy, Johannesburg, South Africa.

Hofmann, G., L. Scheepers, and H. Ogasawara (2013), Loading conditions of geological faults in deep level tabular mines, in *Proceedings of the 6th International Symposium on In-Situ Rock Stress, 20–22 August 2013, Sendai, Japan*, pp. 558–580, Japanese Committee for Rock Mechanics, Tokyo.

Jones, L. M., and P. Molnar (1979), Some characteristics of foreshocks and their possible relationship to earthquake prediction and premonitory slip on faults, *J. Geophys. Res.*, *84*, 3596–3608, doi:10.1029/JB084iB07p03596.

Jouinaux, L., K. Masuda, X. Lei, O. Nishizawa, K. Kusunose, L. Liu, and W. Ma (2001), Comparison of the microfracture localization in granite between fracturation and slip of a preexisting macroscopic healed joint by acoustic emission measurements, *J. Geophys. Res.*, *106*, 8687–8698, doi:10.1029/2000JB900411.

Kato, A., K. Obara, T. Igarashi, H. Tsuruoka, S. Nakagawa, and N. Hirata (2012), Propagation of slow slip leading up to the 2011 Mw 9.0 Tohoku-oki earthquake, *Science*, *315*, 706–708.

Katsura, T. (2009), Rock mass deformation before, at and after an M2.1 earthquake within only 20 m from two Ishii strainmeters [in Japanese], BSc thesis, Ritsumeikan Univ.

Kurita, K., P. L. Swanson, I. C. Getting, and H. Spetzler (1983), Surface deformation of westerly granite during creep, *Geophys. Res. Lett.*, *10*, 75–78, doi:10.1029/GL010i001p00075.

Kwiatek, G., K. Plenkers, M. Nakatani, Y. Yabe, G. Dresen, and JAGURAS-Group (2010), Frequency-magnitude characteristics down to magnitude −4.4 for induced seismicity recorded at Mponeng gold mine, South Africa, *Bull. Seismol. Soc. Am.*, *100*, 1165–1173, doi:10.1785/0120090277.

Lei, X. (2003), How do asperities fracture? An experimental study of unbroken asperities, *Earth Planet. Sci. Lett.*, *213*, 347–359, doi:10.1016/S0012-821X(03)00328-5.

Lei, X., K. Kusunose, M. V. M. S. Rao, O. Nishizawa, and T. Satoh (2000), Quasi-static fault growth and cracking in homogeneous brittle rock under triaxial compression using acoustic emission monitoring, *J. Geophys. Res.*, *105*, 6127–6139, doi:10.1029/1999JB900385.

Lei, X., K. Kusunose, T. Satoh, and O. Nishizawa (2003), The hierarchical rupture process of a fault: An experimental study, *Phys. Earth Planet. Inter.*, *137*, 213–228, doi:10.1016/S0031-9201(03)00016-5.

Lei, X., K. Masuda, O. Nishizawa, L. Jouniaux, L. Liu, W. Ma, T. Satoh, and K. Kusunose (2004), Detailed analysis of acoustic emission activity during catastrophic fracture of faults in rock, *J. Struct. Geol.*, *26*, 247–258, doi:10.1016/S0191-8141(03)00095-6.

Lockner, D. (1993), The role of acoustic emission in the study of rock fracture, *Int. J. Rock Mech. Min. Sci. Geomech. Abstr.*, *30*, 883–899, doi:10.1016/0148-9062(93)90041-B.

Lockner, D., and J. Byerlee (1977), Acoustic emission and creep in rock at high confining pressure and differential stress, *Bull. Seismol. Soc. Am.*, *67*, 247–258.

Manthei, G. (2005), Characterization of acoustic emission sources in a rock salt specimen under triaxial compression, *Bull. Seismol. Soc. Am.*, *95*, 1674–1700, doi:10.1785/0120040076.

McLaskey, C. M., and D. Lockner (2014), Preslip and cascade processes initiating laboratory stick slip, *J. Geophys. Res. Solid Earth*, *119*, 6323–6336, doi:10.1002/2014JB011220.

Mendecki, A. J. (1996), *Seismic Monitoring in Mines*, edited by A. J. Mendecki, 280 pp., Springer, Dordrecht, Netherlands.

Nakatani, M., Y. Yabe, J. Phillipp, G. Morema, S. Stanchits, G. Dresen, and JAGUARS-Group (2008), Acoustic emission measurements in a deep gold mine in South Africa—Project overview and some typical waveforms, *Seismol. Res. Lett.*, *79*, 311.

Naoi, M. (2009), Acoustic emission measurements in the vicinity of a M2 earthquake rupture in a deep gold mine in South Africa [in Japanese], PhD thesis, 140 pp., Univ. of Tokyo.

Naoi, M., M. Nakatani, Y. Yabe, G. Kwiatek, T. Igarashi, and K. Plenkers (2011), Twenty thousand aftershocks of a very small (M 2) earthquake and their relation to the mainshock rupture and geological structures, *Bull. Seismol. Soc. Am.*, *101*, 2399–2407, doi:10.1785/0120100346.

Naoi, M., et al. (2014), Frequency-magnitude distribution of $-3.7 \leq Mw \leq 1$ mining-induced earthquakes around a mining front and *b* value invariance with post-blast time, *Pure Appl. Geophys.*, *171*, 2665–2684, doi:10.1007/s00024-013-0721-7.

Naoi, M., et al. (2015a), Quasi-static slip patch growth to 20 m on a geological fault inferred from acoustic emissions in a South African gold mine, *J. Geophys. Res. Solid Earth*, *120*, 1692–1707, doi:10.1002/2014JB011165.

Naoi, M., et al. (2015b), Steady activity of microfractures on geological faults loaded by mining stress, *Tectonophysics*, *649*, 100–114, doi:10.1016/j.tecto.2015.02.025.

Nishizawa, O., K. Onai, and K. Kusunose (1985), Hypocenter distribution and focal mechanism of AE events during two stress stage creep in Yugawara andesite, *Pure Appl. Geophys.*, *112*, 36–52.

Noda, H., M. Nakatani, and T. Hori (2013), Large nucleation before large earthquakes is sometimes skipped due to cascade-up—Implications from a rate and state simulation of faults with hierarchical asperities, *J. Geophys. Res. Solid Earth*, *118*, 2924–2952, doi:10.1002/jgrb.50211.

Ogasawara, H., T. Katsura, G. Hofmann, Y. Yabe, H. Ishii, D. Roberts, S. Nakao, M. Okubo, A. K. Ward, and H. Kawakata (2013), The Ishii strainmeters to in-situ monitor rock mass response to mining in South African gold mines, in *Proceedings of the 6th South African Rock Engineering Symposium (SARES), 12–14 May 2014*, pp. 21–33, Southern African Institute of Mining and Metallurgy, Johannesburg, South Africa.

Ogasawara, H., H. Kato, G. Hofmann, D. Roberts, P. Piper, T. Clements, A. K. Ward, Y. Yabe, H. Yilmaz, and R. J. Durrheim (2014), BX CCBO in-situ stress measurements at earthquake prone areas in South African gold mines—A summary of mini-workshop on 13 Feb 2014, paper ARMA-2014-7438 presented at 48th U.S. Rock Mechanics/Geomechanics Symposium, Univ. of Minnesota, Minneapolis, Minnesota, 1–4 June.

Ohnaka, M. (1992), Earthquake source nucleation: A physical model for short-term precursors, *Tectonophysics*, *211*, 149–178, doi:10.1016/0040-1951(92)90057-D.

Ohnaka, M. (2004), Earthquake cycles and physical modeling of the process leading up to a large earthquake, *Earth Planets Space*, *56*, 773–793.

Ohnaka, M., and Y. Kuwahara (1990), Characteristic features of local breakdown near a crack-tip in the transition zone from nucleation to unstable rupture during stick-slip shear failure, *Tectonophysics*, *175*, 197–220, doi:10.1016/0040-1951(90)90138-X.

Ohnaka, M., and L. Shen (1999), Scaling of the shear rupture process from nucleation to dynamic propagation: Implications of geometric irregularity of the rupturing surfaces, *J. Geophys. Res.*, *104*, 817–844, doi:10.1029/1998JB900007.

Okada, T., A. Hasegawa, J. Suganomata, N. Umino, H. Zhang, and C. H. Thurber (2007), Imaging the heterogeneous source area of the 2003 M6.4 northern Miyagi earthquake, NE Japan, by double-difference tomography, *Tectonophysics*, *430*, 67–81, doi:10.1016/j.tecto.2006.11.001.

Okubo, P. G., and J. H. Dieterich (1984), Effects of physical fault properties on frictional instabilities produced on simulated faults, *J. Geophys. Res.*, *89*, 5817–5827, doi:10.1029/JB089iB07p05817.

Powers, P., and T. Jordan (2010), Distribution of seismicity across strike-slip faults in California, *J. Geophys. Res.*, *115*, B05305, doi:10.1029/2008JB006234.

Ray, D., C. Mevel, and R. Banerjee (2009), Hydrothermal alteration studies of gabbros from Northern Central Indian Ridge and their geodynamic implications, *J. Earth Syst. Sci.*, *118*, 659–676.

Rice, J. R. (1993), Spatio-temporal complexity of slip on a fault, *J. Geophys. Res.*, *98*, 9885–9907, doi:10.1029/93JB00191.

Richardson, E., and T. E. Jordan (2002), Seismicity in deep gold mines of South Africa: Implications for tectonic earthquakes, *Bull. Seismol. Soc. Am.*, *92*, 1766–1782, doi:10.1785/0120000226.

Satoh, T., K. Shivakumar, O. Nishizawa, and K. Kusunose (1996), Precursory localization and development of microfractures along the ultimate fracture plane in amphibolite under triaxial creep, *Geophys. Res. Lett.*, *23*, 865–868, doi:10.1029/96GL00739.

Shibazaki, B., and M. Matsu'ura (1998), Transition process from nucleation to high-speed rupture propagation: Scaling from stick-slip experiments to natural earthquakes, *Geophys. J. Int.*, *132*, 14–30, doi:10.1046/j.1365-246x.1998.00409.x.

Thompson, B. D., R. P. Young, and D. A. Lockner (2005), Observations of premonitory acoustic emission and slip nucleation during a stick slip experiment in smooth faulted Westerly granite, *Geophys. Res. Lett.*, *32*, L10304, doi:10.1029/2005GL022750.

Thompson, B. D., R. P. Young, and D. A. Lockner (2006), Fracture in Westerly granite under AE feedback and constant strain rate loading: Nucleation, quasi-static propagation, and the transition to unstable fracture propagation, *Pure Appl. Geophys.*, *163*, 995–1019, doi:10.1007/s00024-006-0054-x.

Umino, N., T. Okada, and A. Hasegawa (2002), Foreshock and aftershock sequence of the 1998 M 5.0 Sendai, northeastern Japan, earthquake and its implications for earthquake nucleation, *Bull. Seismol. Soc. Am.*, *92*, 2465–2477, doi:10.1785/0120010140.

Wessel, P., and W. Smith (1991), Free software helps map and display data, *Eos Trans. AGU*, *72*, 441, doi:10.1029/90EO00319.

Yabe, Y., N. Kato, K. Yamamoto, and T. Hirasawa (2003), Effect of sliding rate on the activity of acoustic emission during stable sliding, *Pure Appl. Geophys.*, *160*, 1163–1189, doi:10.1007/s000240300000.

Yabe, Y., J. Philipp, M. Nakatani, G. Morema, M. Naoi, H. Kawakata, T. Igarashi, G. Dresen, H. Ogasawara, and JAGUARS (2009), Observation of numerous aftershocks of an Mw 1.9 earthquake with an AE network installed in a deep gold mine in South Africa, *Earth Planets Space*, *61*, e49–e52.

Yabe, Y., et al. (2013), Estimation of the stress state around the fault source of a Mw 2.2 earthquake in a deep gold mine in South Africa based on borehole breakout and core discing, in *Proceedings of the 6th International Symposium on In-Situ Rock Stress, 20–22 August 2013, Sendai, Japan*, pp. 604–613, Japanese Committee for Rock Mechanics, Tokyo.

Yamaoka, K., T. Ooida, and Y. Ueda (1999), Detailed distribution of accelerating foreshocks before a M 5.1 earthquake in Japan, *Pure Appl. Geophys.*, *155*, 335–353, doi:10.1007/978-3-0348-8677-2_7.

Yanagidani, T., S. Ehara, O. Nishizawa, K. Kusunose, and M. Terada (1985), Localization of dilatancy in Oshima granite under constant uniaxial stress, *J. Geophys. Res.*, *90*, 6840–6858, doi:10.1029/JB090iB08p06840.

Young, R. P., J. F. Hazzard, and W. S. Pettitt (2000), Seismic and micromechanical studies of rock fracture, *Geophys. Res. Lett.*, *27*, 1767–1770, doi:10.1029/2000GL011547.

Yukutake, Y., T. Takeda, and K. Obara (2008), Fine fault structure of a moderate earthquake in the 2007 earthquake sequence of northern Mie, Japan, *Earth Planets Space*, *60*, 981–985.